ELSEVIER

Rayleigh–Taylor instabilities from hydration and melting propel 'cold plumes' at subduction zones

Taras V. Gerya [a,b,*], David A. Yuen [c]

[a] *Institut für Geologie, Mineralogie und Geophysik, Ruhr-Universität Bochum, 44780 Bochum, Germany*
[b] *Institute of Experimental Mineralogy, Russian Academy of Sciences, 142432 Chernogolovka, Moscow, Russia*
[c] *University of Minnesota Supercomputing Institute and Department of Geology and Geophysics, University of Minnesota, Minneapolis, MN 55455-0219, USA*

Abstract

It is commonly thought that hot diapiric flows prevail in the mantle wedge above the subducting slab. However, hydration and partial melting along the slab can create a situation in which a Rayleigh–Taylor instability can develop at the top of a cold subducting slab. We have numerically modeled this parodoxically interesting geological phenomenon, in which rising diapiric structures, colder than the asthenosphere by 300–400°C, are driven upward by compositional buoyancy, with a high-resolution two-dimensional regional model. These 'cold plumes' with a compositional, hydrous origin, launched from a depth of greater than 100 km, are lubricated by viscous heating, have an upward velocity in excess of 10 cm/yr, penetrate the relatively hot asthenosphere in the mantle wedge within a couple of million years and thus can cool the surroundings. These 'cold plumes' are fueled by partial melting of the hydrated mantle and subducted oceanic crust due to fluid release from dehydration reactions wihin the slab, including the decomposition of serpentine. There may be a spatial correlation between seismicity and the particular depth of cold-plume initiation.
Published by Elsevier Science B.V.

Keywords: mantle plumes; subduction zones; magmatic activity; seismicity; 2-D numerical modeling

1. Introduction

Today it is well accepted that upwellings in the mantle can be driven by either thermal or chemical buoyancy and they can occur in various morphologies, such as cylindrical structures, diapirically shaped objects (e.g. [1,2]) or even lineated features [3]. Mantle plumes are commonly held to come from either the core–mantle boundary [4,5] or from the transition zone (e.g. [6]). Yet there are engimatic volcanic features near the vicinity of the subducting slab which require their sources to be associated with fluid-dynamic instabilities due to hydration and melting developed on the top layer of the subducting slab [7–15].

However, in contrast to generation of hot mantle upwellings, hydration and related melting

* Corresponding author. Tel.: +49-234-3223518;
Fax: +49-234-3214433.
E-mail address: taras.gerya@ruhr-uni-bochum.de
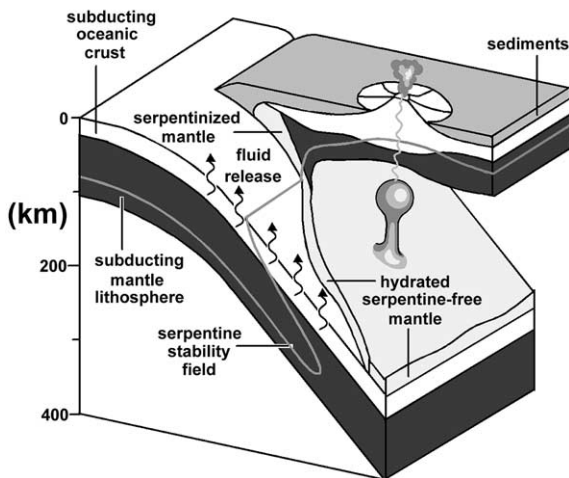(T.V. Gerya).

Fig. 1. Conceptual 3-D model of the cold-plume generation process. See the text for details.

would introduce a source of chemical buoyancy [11,16] on the top of the subducting slab within a relatively cold area characterized by an inverted temperature gradient (e.g. [17,18]). In Fig. 1 we depict a three-dimensional (3-D) conceptual model showing the dynamical outcome from this unusual thermal–chemical situation. This extraordinary background is caused by the colder subducting lithosphere consisting of an intrinsically lighter hydrated peridotite lying underneath a hotter but compositionally heavier dry overlying mantle. 3-D diapiric structures are suggested to form from thermal–chemical instabilities developed at a depth of around 100–200 km, as a result of the dehydration of serpentines and the subsequent hydration reactions involving peridotites (e.g. [19]).

In this paper we will investigate from two-dimensional (2-D) numerical modeling this geodynamically plausible scenario of cold but compositionally lighter plumes emerging from the upper surface of the slab due to a supercritically unstable situation in thermal–chemical convection (e.g. [20]).

2. Initial and boundary conditions of the 2-D model

From our 3-D conceptual model we have de-

signed a regional 2-D model that takes into account the process of hydration of the mantle wedge by the fluid released from a kinematically prescribed subducting plate. Fig. 2 shows the initial (panel a) and boundary (panel b) conditions and the hydration model used (panel c). We assume that dehydration of the subducting slab liberates an upward migration of aqueous fluid, resulting in the hydration of the mantle wedge near the slab (see panel c). The hydration leads to a sharp decrease in density and viscosity of mantle rocks, creating favorable conditions for the development of a compositionally driven Rayleigh–Taylor instability along the propagating hydration front (Figs. 1 and 2). This compositional difference arises from the water contents.

We used a realistic (e.g. [21]) layered structure of 8 km thick subducting oceanic crust (Fig. 2a) composed of sedimentary (1 km), basaltic (2 km) and gabbroic (5 km) layers characterized by different physical properties (Table 1). The initial position of the subduction zone (Fig. 2a) is prescribed by an 8 km thick weak layer (e.g. [29,30]) composed of hydrated peridotite [31]. During subduction, this layer is spontaneously substituted by weak subducted crustal rocks and hydrated mantle, implying a decoupling along the plate interface (e.g. [32]). The initial temperature field in the subducting plate, with a uniform descending rate of 2 cm/yr (Fig. 2a), is defined by an oceanic geotherm $T_0(z)$ due to a cooling half-space model with a specified age. The initial temperature distribution in the overriding plate corresponds to the equilibrium thermal profile with 0°C at the surface and 1350°C at 32 km depth.

The kinematic boundary conditions (Fig. 2b) correspond to the corner flow model (e.g. [33,34]) and simulate asthenospheric mantle flow at temperatures exceeding 1000°C in the mantle wedge (e.g. [9,25,29]). To ensure a smooth continuity of the temperature field across the lower boundary of the truncated regional model, we have used a boundary condition involving the vanishing changes of the vertical Lagrangian heat flux, q_z, with depth ($\partial q_z/\partial z = 0$) [35].

The top surface is calculated dynamically at each time step like a free surface (e.g. [36,37]). To account for the changes in the topography

we used a layer with a lower viscosity (10^{18} Pa s) whose initial thickness is 8 km on the top of the oceanic crust. The density of this layer is taken to be 1 kg/m^3 (air) at $z < 4$ km and 1000 kg/m^3 (sea water) at $z > 4$ km. An interface between this layer and the top of the oceanic crust is considered to be the erosion/sedimentation surface, which evolves according to the following transport equation solved at each time step:

$$\partial z_{es}/\partial t = v_z - v_x \partial z_{es}/\partial x - v_s + v_e \tag{1}$$

where z_{es} is the vertical position of the surface as a function of the horizontal distance, x; v_z and v_x are the vertical and horizontal components of the material velocity vector at the surface; v_s and v_e are, respectively, sedimentation and erosion rates corresponding to the relation:

$$v_s = 0 \text{ mm/a}, \ v_e = 1 \text{ mm/a when } z < 4 \text{ km},$$

$$v_s = 0.3 \text{ mm/a}, \ v_e = 0 \text{ mm/a when } z > 4 \text{ km}$$

3. Dehydration and hydration models

To account for the effects of hydration processes (Fig. 2c) in a viscous medium, we describe the vertical displacement of the hydration front (i.e. the interface between hydrated and dry mantle rock) with respect to the upper surface of the subducting slab (in Eulerian coordinates) by the following transport equation [25] solved at each time step:

$$\partial z_h/\partial t = v_z - v_x \partial z_h/\partial x - v_h \tag{2}$$

where z_h is the vertical location of the hydration front as a function of the horizontal distance, x, measured from the trench; v_h is the hydration rate; v_z and v_x are the vertical and horizontal components of the material velocity vector at the front.

In a situation where the availability of water controls the progress of the mantle hydration (e.g. [38]), spatial changes in the hydration rate along the hydration front should mainly depend on spatial changes in the rate of fluid release along the surface of the subducting plate. Following a continuous dehydration model [27] for the subducting lithosphere, we assume that the rate of fluid release along the slab and, consequently, the hydration rate can be roughly approximated by a linear function of the horizontal distance, x, measured from the trench (Fig. 2c):

$$v_h/v_s = A[1 - Bx/x_{lim}] \quad \text{when } x < x_{lim},$$

$$v_h/v_s = 0 \quad \text{when } x > x_{lim} \tag{3}$$

where v_s is the subduction rate; x_{lim} is the limiting horizontal distance from the trench (Fig. 2c), to the right of which fluid release from the subducting plate is negligible [25]. The non-dimensional parameter B may vary from -1 to 1, characterizing either the increase ($B < 0$) or the decrease ($B > 0$) in hydration rate with depth. The parameter A is a non-dimensional intensity in the hydration process of the mantle wedge. Typical values of the parameter A range between 0.01 and 0.30 as a function of (i) the water contents in the hydrated peridotite and (ii) the total amount of water released from the subducting plate by the limiting distance x_{lim} [25].

From experimental data [27] the major hydrous phases stable in peridotite at depths < 200 km are serpentine, talk, chlorite, amphibole and free pore fluid. The amount of water consumed by the hydrous minerals [27] is variable (0.2–6.6 wt%) and reach a maximum for serpentine-bearing assemblages (3.9–6.6 wt%). At depths > 60 km and temperatures > 850°C dense supercritical water–silicate fluid(melt) is the only hydrous phase stable in peridotite (e.g. [27,39]). Our hydration model assumes slow percolation rate and large volumetric fraction of this supercritical fluid in hydrated peridotite, implying high (1–3 wt%) bulk rock water content and large (100–200 kg/m^3) density contrast with dry mantle [11]. This is related to the high solubility of the silicate component increasing fluid viscosity and density at high pressure and temperature (e.g. [39,40]).
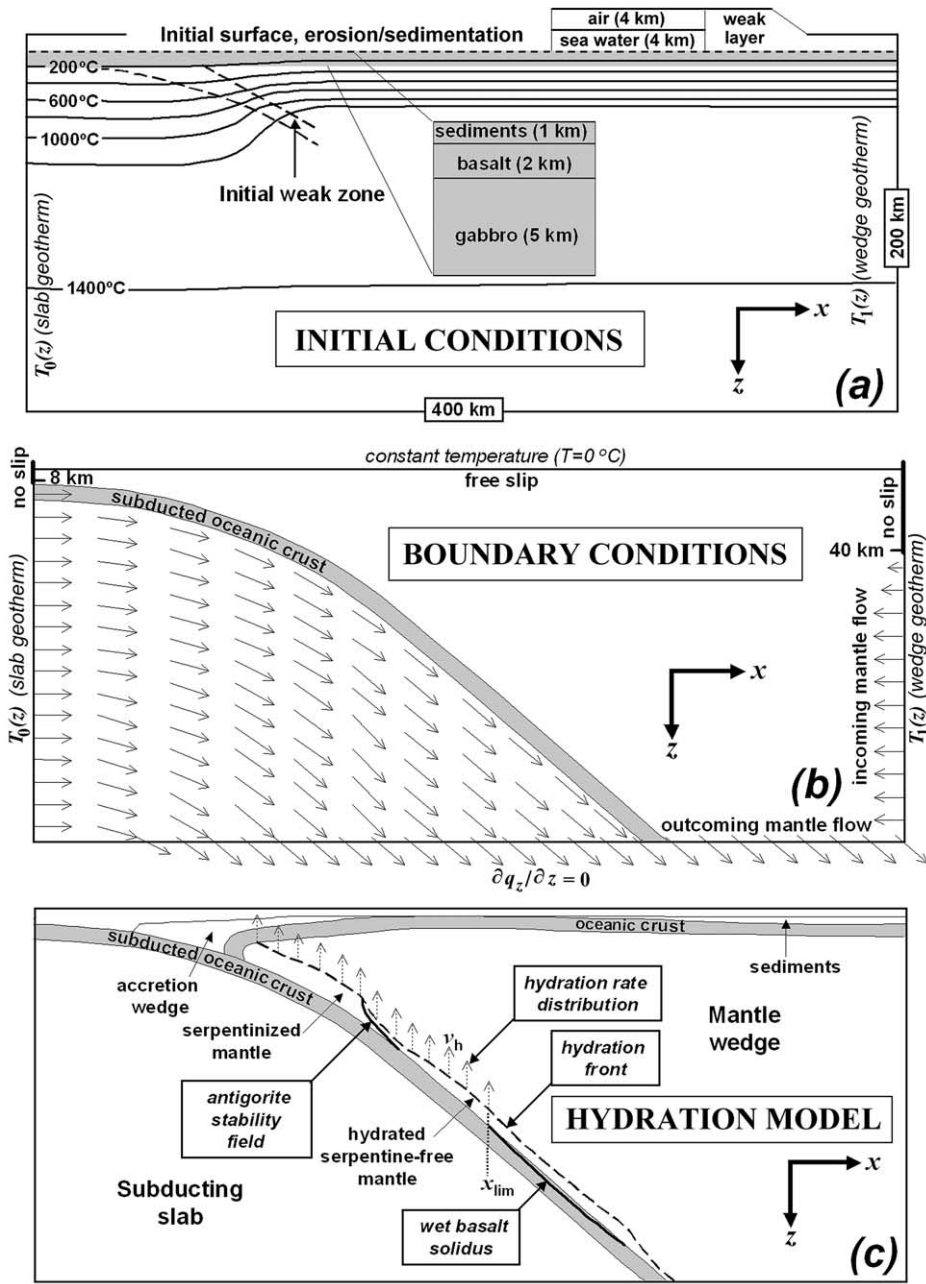
Fig. 2. Design of (a) initial, (b) boundary conditions and (c) hydration model of the mantle wedge used in our 2-D numerical experiments. See the text for details.

4. Partial melting model

According to the adopted melting model [22], melting of hydrated peridotite and subducted

rocks occurs in the P–T region between the corresponding wet solidus and dry liquidus of these petrological components (Table 1). As a first approximation, the degree of melting is taken to

Table 1
Material properties[a] used in 2-D numerical experiments

Material	ρ_0 (kg/m^3)	R_ρ [b]	k (W/m K)	Rheology (solid rocks)	T_{solidus} (K)	T_{liquidus} (K)	H_L (kJ/kg)	H_r (10^{-6} W/m^3)
Sedimentary rocks	2700–3000 (solid), 2400 (molten)	15.2–7.6 (solid), 22.7 (molten)	0.64+807/ (T+77)	constant viscosity, 10^{19} Pa s	889+17 900/(P+54)+20 200/(P+54)^2 at $P < 1200$ MPa, 831+0.06P at $P > 1200$ MPa	1262+0.09P	300	2
Basaltic crust	3100–3200 (solid), 2900 (molten)	5.1–2.5 (solid), 10.1 (molten)	1.18+474/ (T+77)	constant viscosity, 10^{19} Pa s	973−70 400/(P+354)+77 800 000/ (P+354)^2 at $P < 1600$ MPa, 935+0.0035P+0.0000062P^2 at $P > 1600$ MPa	1423+0.105P	380	0.25
Gabbroic crust	–//–	–//–	–//–	An$_{75}$ flow law, $\lambda = 0.9$	–//–	–//–	–//–	–//–
Serpentinized mantle	3000	7.6	0.73+1293/ (T+77)	constant viscosity, 10^{19} Pa s	–	–	–	0.022
Hydrated unser- pentinized mantle[c]	3200 (solid), 3000 (molten)	2.5 (solid), 7.6 (molten)	–//–	wet olivine flow law, $\lambda = 0.9$	1240+49 800/(P+323) at $P < 2400$ MPa, 1266−0.0118P+0.0000035P^2 at $P > 2400$ MPa	2073+0.114P	400	–//–
Dry mantle	3300	0	–//–	dry olivine flow law, $\lambda = 0$	–	–	–	–//–
References	[21,22]		[23]	[24,25]	[26–28]	[26–28]	[21,22]	[21]

[a] $Cp = 1000$ J/kg, $\alpha = 3 \times 10^{-5}$ K^{-1}, $\beta = 1 \times 10^{-5}$ Mpa^{-1} for all types of rocks.

[b] $R_\rho = (\rho_r - \rho_0)/(\rho_r \alpha \Delta T)$, where $\rho_r = 3300$ kg/m^3 is the reference density of dry mantle, $\Delta T = 400$ K is the temperature difference for the asthenospheric portion of the mantle wedge.

[c] Hydrated mantle beyond the antigorite stability field [27]: $T > 751+0.18P−0.000031P^2$ at $P < 2100$ MPa, $T > 1013−0.0018P−0.0000039P^2$ at $P > 2100$ Mpa.

increase linearly with the temperature according to the relations:

$$M = 0 \text{ at } T < T_{\text{solidus}} \tag{4a}$$

$$M = (T - T_{\text{solidus}})/(T_{\text{liquidus}} - T_{\text{solidus}})$$
$$\text{at } T_{\text{solidus}} < T < T_{\text{liquidus}} \tag{4b}$$

$$M = 1 \text{ at } T > T_{\text{liquidus}} \tag{4c}$$

where M is the volumetric fraction of melt with temperature; T_{solidus} and T_{liquidus} are, respectively, wet solidus and dry liquidus temperature at given pressure and rock composition (Table 1).

An effective density, ρ_{eff}, of partially molten rocks is calculated from the formula:

$$\rho_{\text{eff}} = \rho_{\text{solid}} - M(\rho_{\text{solid}} - \rho_{\text{molten}}) \tag{5}$$

where ρ_{solid} and ρ_{molten} are, respectively, densities of solid and molten rock varying with pressure and temperature according to the relation:

$$\rho_{P,T} = \rho_0 \left[1 - \alpha(T - T_0)\right]\left[1 + \beta(P - P_0)\right] \tag{6}$$

where ρ_0 is the standard density at $P_0 = 0.1$ MPa and $T_0 = 298$ K; α and β are, respectively, the thermal expansion and compressibility coefficients.

The effects of latent heating are accounted for by an increased effective heat capacity of partially molten rocks (Cp_{eff}) calculated according to the equation:

$$Cp_{\text{eff}} = Cp + H_{\text{L}}/(T_{\text{liquidus}} - T_{\text{solidus}}) \tag{7}$$

where Cp is heat capacity of the rock assemblage; H_{L} is latent heat of melting for the lithological unit, J/kg.

5. Rheological model

At temperatures lower than about 700 K the creep rheology for the solid rocks ($M < 0.1$) is combined with a quasi-brittle rheology to yield an effective rheology [41]. For this purpose the Mohr–Coulomb law [24,42] is simplified to the yield stress, σ_{yield} criterion and implemented by a 'Mohr–Coulomb viscosity', η_{MC} as follows:

$$\eta_{\text{MC}} = \sigma_{\text{yield}}/(4\varepsilon_{\text{II}})^{1/2}, \ \sigma_{\text{yield}} =$$
$$(M_1 P_{\text{lith}} + M_2)(1 - \lambda) \tag{8}$$

where $\varepsilon_{\text{II}} = 1/2\varepsilon_{ij}\varepsilon_{ij}$ is the second invariant of the strain rate tensor, with dimension s^{-2}; $\lambda = P_{\text{fluid}}/P_{\text{lith}}$ is the pore fluid pressure coefficient, i.e. the ratio between pore fluid pressure, P_{fluid}, and lithostatic pressure, P_{lith}; M_1 and M_2 (MPa) are empirical constants ($M_1 = 0.85$, $M_2 = 0$ MPa when $\sigma_{\text{yield}} < 200$ MPa and $M_1 = 0.6$, $M_2 = 60$ MPa when $\sigma_{\text{yield}} > 200$ MPa [42]). The total effective viscosity, η, is then defined by the following criterion:

$$\eta = \eta_{\text{creep}} \text{ when } 2(\varepsilon_{\text{II}})^{1/2} \ \eta_{\text{creep}} < \sigma_{\text{yield}} \tag{9a}$$

$$\eta = \eta_{\text{MC}} \text{ when } 2(\varepsilon_{\text{II}})^{1/2} \ \eta_{\text{creep}} > \sigma_{\text{yield}} \tag{9b}$$

where η_{creep} is the creep viscosity, Pa s. The creep viscosity, depending on the stress and temperature, is defined in terms of deformation invariants by [24]:

$$\eta_{\text{creep}} = (\varepsilon_{\text{II}})^{(1-n)/2n} F(A_{\text{D}})^{-1/n} \exp(E/nRT) \tag{10}$$

where F, A_{D}, E and n are flow law parameters determined experimentally [24].

High-pressure metamorphic rocks exhumed from subduction zones reveal little evidence of dislocation deformation of their principal minerals at depths from 40 to 150 km [43,44]. Therefore, a constant Newtonian creep viscosity $\eta_{\text{creep}} = 10^{19}$ Pa s [25] is assigned to the subducted sediment, the upper hydrated portion of the basaltic oceanic crust, and to the serpentinized mantle, while a power-law rheology is used for the lower gabbroic portion of the oceanic crust and for the unserpentinized mantle material (Table 1).

The effective viscosity, η, of molten rocks ($M > 0.1$) was calculated by using the following formula [22,45]:

$$\eta = \eta_{\text{o}} \exp\{2.5 + [(1 - M)/M]^{0.48}(1 - M)\} \tag{11}$$

where $\eta_{\text{o}} = 10^{13}$ Pa s ($\eta = 1 \times 10^{14}$–2×10^{15} Pa s) is taken for the basic oceanic crust and hydrated

peridotite and $\eta_o = 5 \times 10^{14}$ Pa s ($\eta = 6 \times 10^{15}$–8×10^{16} Pa s) is used for the felsic sedimentary rocks [22].

6. Mathematical modeling and numerical implementation

We have considered 2-D creeping flow wherein both thermal and chemical buoyant forces are included. The conservation of mass is approximated by the incompressible continuity equation:

$$\partial v_x / \partial x + \partial v_z / \partial z = 0 \qquad (12)$$

The 2-D Stokes equations take the form:

$$\partial \sigma_{xx}/\partial x + \partial \sigma_{xz}/\partial z = \partial P/\partial x \qquad (13)$$

$$\partial \sigma_{zz}/\partial z + \partial \sigma_{xz}/\partial x = \partial P/\partial z - g\rho(T,C,M) \qquad (14)$$

The density $\rho(T,C,M)$ depends explicitly on the temperature, the composition, and the degree of melting (see Section 4). We do not explicitly consider the sub-grid process of percolation of melts (e.g. [46]) and aqueous fluids, which would require a different set of governing equations (e.g. [47,48]). For the thermal–chemical convection problem [20] modeled here the buoyancy ratio R_ρ is defined as $\Delta\rho/(\rho_r\alpha\Delta T)$, where $\Delta\rho$ is the compositional change from the reference density ρ_r (the standard density of dry mantle rock, 3300 kg m^{-3}), ΔT is the temperature difference for the convecting region ($\Delta T = 400$ K for the asthenospheric portion of the mantle wedge).

We also employ realistic rheological constitutive relationships between the stress and strain rate, whose coefficient η represents the effective viscosity, which depends on the composition, temperature, pressure, strain rate and degree of melting (see Section 5)

$$\sigma_{xx} = 2\eta\varepsilon_{xx}, \ \sigma_{xz} = 2\eta\varepsilon_{xz}, \ \sigma_{zz} = 2\eta\varepsilon_{zz},$$

$$\varepsilon_{xx} = \partial v_x/\partial x, \ \varepsilon_{xz} = 1/2(\partial v_x/\partial z + \partial v_z/\partial x),$$

$$\varepsilon_{zz} = \partial v_z/\partial z$$

We have adopted [49] a Lagrangian frame of

reference in which the temperature equation with a temperature-dependent thermal conductivity $k(T)$ (Table 1) takes the form:

$$\rho Cp(\mathrm{D}T/\mathrm{D}t) = \partial q_x/\partial x + \partial q_z/\partial z + H_r + H_a + H_s,$$

$$q_x = k(T)(\partial T/\partial x), \ q_z = k(T)(\partial T/\partial z),$$

$$H_r = \text{constant}, \ H_a =$$

$$T\alpha[v_x(\partial P/\partial x) + v_z(\partial P/\partial z)] \approx T\alpha\rho v_z g, \ H_s =$$

$$\sigma_{xx}\varepsilon_{xx} + \sigma_{zz}\varepsilon_{zz} + 2\sigma_{xz}\varepsilon_{xz} \qquad (15)$$

where D/Dt represents the substantive time derivative.

The notations in Eqs. 12–15 are: x and z denote, respectively, the horizontal and vertical coordinates, in m, v_x and v_z are components of velocity vector v in m/s; t, time in s; σ_{xx}, σ_{xz}, σ_{zz} are components of the viscous deviatoric stress tensor in Pa; ε_{xx}, ε_{xz}, ε_{zz} are components of the strain rate tensor in s^{-1}; P, the pressure in Pa; T, the temperature in K; q_x and q_z are heat fluxes in W/m^2; η, the effective viscosity in Pa s; ρ, the density in kg/m^3; $g = 9.81$ m/s^2 is the gravitational vector; k is the thermal conductivity in W/(m K); Cp is the isobaric heat capacity in J/(kg K); H_r, H_a and H_s denote, respectively, radioactive, adiabatic and shear heat production in W/m^3.

We have employed a recently developed 2-D code (I2VIS) based on finite differences with a marker technique allowing for the accurate conservative solution of the governing equations on a rectangular, fully staggered Eulerian grid for multiphase viscoplastic flow [49]. A detailed description of the numerical method and algorithmic tests is provided in Gerya and Yuen [49].

7. Numerical and visualization results

All models (Table 2) have been calculated on a finite-difference grid of 200×100 regularly spaced Eulerian points and with 500 000 markers for portraying the fine details of the temperature, material and viscosity fields. Lateral viscosity contrasts, up to 10^7, are maintained in the models shown

here. The complex realistic material set-up (Table 1 and Fig. 3) of our model reflects variability of subducted chemical components participating in the global mantle convection process (e.g. [50]).

We studied generation of cold plumes in numerical experiments with both moderate ($\Delta\rho = 140$ kg/m^3, $R_\rho = 3.5$; see Models 1–4 in Table 2) and high ($\Delta\rho = 220$ kg/m^3, $R_\rho = 5.6$; see Models 5–10 in Table 2) initial density contrast between the hydrated source layer and the mantle wedge. The changes in $\Delta\rho$ and R_ρ are related to assumed variations (Tables 1 and 2) in the standard density of solid sedimentary rocks (2700–3000 kg/m^3) and oceanic crust (3100–3200 kg/m^3) composing a significant volume of the source layer (Fig. 3 and Table 2) as a result of dynamic mixing of rocks in serpentinized channels [25]. The initial values of $\Delta\rho$ and R_ρ do not take into account the influence of melting and define early stages of cold-plume growth. During the propagation of cold plumes in the mantle wedge both the density contrast and the buoyancy ratio in-

crease, reaching maximum values of $\Delta\rho = 400$ kg/m^3 and $R_\rho = 10$ (Table 2) as a result of melting (see P–T diagram in Fig. 3).

In Fig. 3 we show the temperature field portrayed as isotherms and the distinct lithologic structures of the subducted oceanic crust and melt in the left-hand column of Fig. 3 and the effective viscosity+velocity fields in the right-hand column, with the sequence of events going from top to bottom for the model with moderate initial buoyancy ratio $R_\rho = 3.5$ (Model 1 in Table 2). Henceforth, we will refer to Figs. 3 and 4 as the reference model.

The initial stages, younger than 25 Ma, are characterized by the progressive hydration of the mantle wedge resulting in the propagation of the hydration front (light bright-blue+light gray-blue) from the subducting slab. The hydrated mantle is clearly subdivided into two parts: an upper, serpentinized subduction channel (light gray-blue) developing within an upper, colder, lithospheric portion of the wedge and a lower, hydrated ser-

Table 2
Parameters[a] of selected numerical experiments

Model	Figure	Hydration parameters	Age of subducting slab (Myr)	Shear heating	ρ_0 for solid oceanic crust (kg/m^3)	ρ_0 for solid sedimentary rock (kg/m^3)	Initial/ maximal R_ρ[b]	Time/depth of 'cold-plume' generation (Myr/km)
1 (plut)	3, 4, 5a	$A = 0.05$, $B = 0$	80	at all temperatures	3200	3000	3.5/9.9	32/174, 34/133
2 (plad)	5b	$A = 0.05$, $B = 0$	80	at $T > 600$ K	3200	3000	3.5/9.9	not generated
3 (plae)	5c	$A = 0.05$, $B = 0$	80	no shear heating at all	3200	3000	3.5/9.9	not generated
4 (plai)	–	$A = 0.05$, $B = 0$	80	lowered within the slab[c]	3200	3000	3.5/9.9	not generated
5 (pluy)	–	$A = 0.05$, $B = 0$	80	at all temperatures	3100	2700	5.6/10	19/73, 29/190
6 (pluu)	6a	$A = 0.10$, $B = 0$	80	at all temperatures	3100	2700	5.6/10	19/71, 24/185, 28/109
7 (pluv)	6b	$A = 0.05$, $B = 0$	60	at all temperatures	3100	2700	5.6/10	20/63, 24/86, 28/118
8 (plux)	6c	$A = 0.05$, $B = 0$	80	no shear heating at all	3100	2700	5.6/10	20/126
9 (pluz)	6d	$A = 0.05$, $B = 0$	100	at all temperatures	3100	2700	5.6/10	21/79
10 (plab)	–	$A = 0.10$, $B = 1$	80	at all temperatures	3100	2700	5.6/10	19/53, 22/156

[a] Other parameters of numerical models are: box size, 400 km×200 km; grid resolution, 200×100 regularly spaced points; geometry representation, 500 000 markers; limiting distance for hydration $x_{lim} = 150$ km; subduction rate 2 cm/yr; subduction angle 45°; viscosity variations = 10^{18}–10^{25} Pa s.
[b] Variations in R_ρ depend on changes in the degree of melting, M, during cold plume propagation; we assumed the following average composition of the source layer (Figs. 3, 5, 6): 60 vol% of hydrated peridotite ($M = 0$–0.3), 20 vol% of sedimentary rocks ($M = 0$–1), 20 vol% of oceanic crust ($M = 0$–0.8).
[c] Shear heating is calculated at all temperatures and lowered by using limiting upper value of viscosity 10^{23} Pa s for the slab mantle and gabbroic crust.
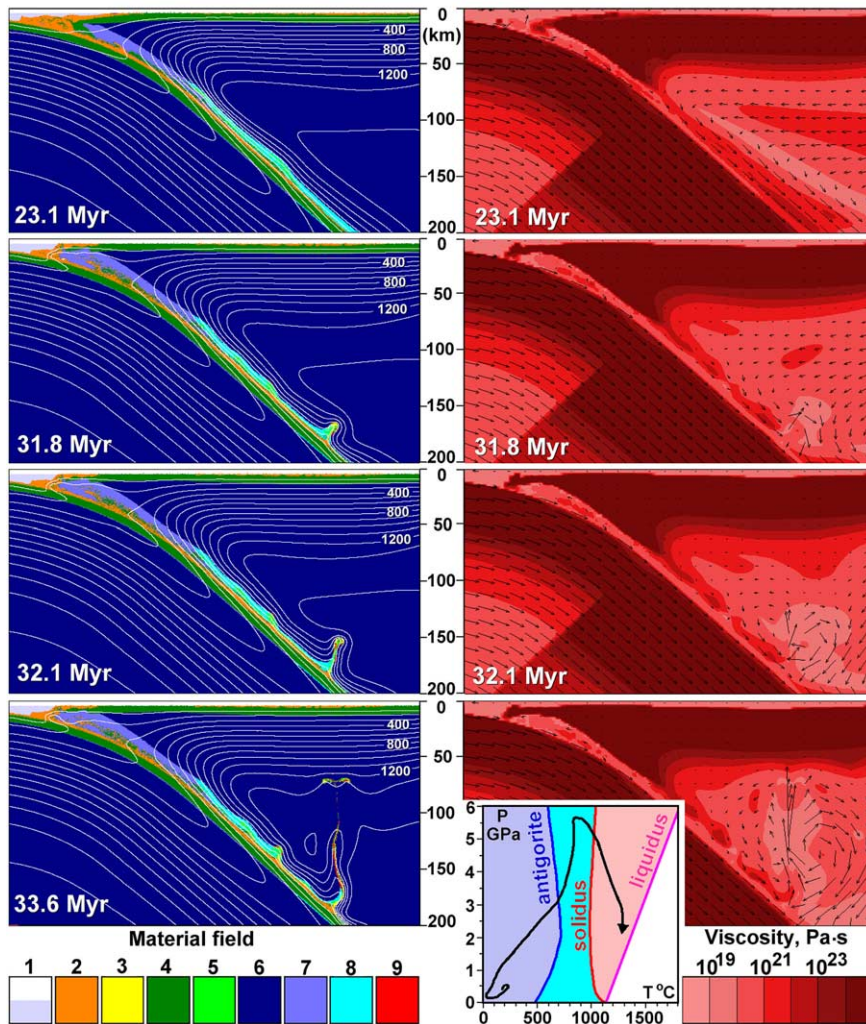
Fig. 3. Development of the geometry of the mantle wedge during ongoing subduction for a reference model with moderate initial buoyancy ratio $R_\rho = 3.5$ (Model 1 in Table 2). The inset separate sketches represent enlarged 320×200 km areas of the original 400×200 km models. Left: Evolution of the temperature field (isotherms labeled in °C) and distribution of rock types (color code): 1, weak layer at the top of the model (see Fig. 2a); 2 and 3, solid and partially molten sedimentary rocks, respectively; 4 and 5, solid and partially molten oceanic crust (both basaltic and gabbroic, see Fig. 2a), respectively; 6, unhydrated mantle; 7, serpentinized mantle; 8, hydrated unserpentinized (i.e. beyond stability field of antigorite, see P–T diagram) mantle; 9, partially molten hydrated mantle. Right: Evolution of viscosity (color code) and velocity field (arrows). P–T diagram shows antigorite stability boundary (solid blue line), wet solidus of peridotite (solid red line) and dry liquidus of basalt (solid magenta line) compared with typical P–T trajectory (solid black line) of rocks composing the cold plume. Color code of P–T diagram corresponds to the stability fields of serpentinized (light gray-blue), hydrated unserpentinized (light bright-blue), and partially molten (light red, white) peridotite, and fully molten basalt (white).

pentine-free peridotite zone (light bright-blue) developing within a lower, hotter asthenospheric portion outside of the P–T stability field of antigorite (see P–T diagram in Fig. 3). These two zones are separated by the zone of narrowing caused by the forced flow of the hot asthenosphere toward the subducting plate, which is controlled by the conservation of mass. The narrowing also produces a wedge-shaped closure of the serpentinized subduction channel, triggering a sec-

ondary flow of serpentinized mantle, sedimentary rocks and oceanic crust within the channel [25]. Mixing of these rocks in the channel contributes to the lithological composition of the subducting hydrated layer atop the slab (Fig. 3).

Afterwards, from 25 to 34 Myr, there emerges a Rayleigh–Taylor instability driven by compositional variations along the upper surface of the serpentine-free (light bright-blue) hydrated peridotite zone. This instability is related to the strong (100–200 kg/m^3) density contrast [11] between the hydrated lower-density layer (i.e. hydrated peridotite partially mixed with sedimentary rocks and oceanic crust) and the higher density of the overriding dry asthenosphere. The density contrast is partially compensated, but not completely canceled, by the significant (300–400°C) temperature difference between the hydrated layer and dry mantle. The initial buoyancy ratio $R_\rho = 3.5$ (Table 2) for these models is very supercritical and chemically dominated.

The diapirs rise upward from the subducting plate and then go up to the hotter mantle wedge. The upward plume velocity can be very significant (around tens of centimeters per year) and exceeds the subduction speed by a long shot. In several numerical experiments most intensive development of the 'cold plumes' may trap significant amounts of subducted oceanic crust and sedimentary rocks from the top of the subducting slab, thus producing a complex mixture of partially molten rocks with both subducted and mantle origins lodged within the wedge. The depth for the appearance of the diapirs (Table 2) is defined by a critical time window (10–20 Myr) available for the growth of the Rayleigh–Taylor instabilities, which are displaced downward along the hydration front by an intense flow. In case of smaller R_ρ, these instabilities do not have enough time to produce plumes at a depth of 200 km.

An interesting point is the development of a pronounced low-viscosity channel at the top of the slab (right-hand column of Fig. 3) and the core of the rising cold plume has a low viscosity because of a strong strain-rate dependence of the viscosity and the partial-melt rheology. The notably higher effective viscosity of the mantle wedge, especially of its colder part in the proximity of the

subducting slab, poses major rheological limitations for rates of generation and propagation of the cold plumes. We note that the viscosity fields simulated in the core of the slab (Fig. 3) cannot be considered to be realistic. This is because of the kinematic nature of the slab velocity boundary conditions, which give rise to sudden changes in the viscosity field due to the sharp transition from the slab bending to the uniform angle subduction. Therefore, we also have not considered in this kinematic boundary condition region the shear heating associated with slab bending (e.g. [51]) in the temperature equation.

In Fig. 4 we display the temperature field (left-hand column) and the distribution of viscous heating (right-hand column). The paradoxical nature of the cold rising plume is illustrated clearer by the upward protrusion of the blue finger in the temperature field. There is a great amount of viscous heating produced by this thermal–chemical plume, due to a decrease in the gravitational potential energy from the rising of lighter material, which in turn is converted efficiently to mechanical heating by the large R_ρ ratio [52–54]. Rising of cold plumes is associated with progressive hydrous melting (see P–T diagram in Fig. 3), increasing both density contrast and buoyancy ratio toward their maximal values of $\Delta\rho = 400$ kg/m^3 and $R_\rho = 10$ (Table 2), also non-linearly increasing the amount of shear heating (Fig. 4). Thus, the rising of cold plumes is accelerated by the feedback from progressive melting caused by shear and conductive heating and decompression [11,55].

We focus our attention on the influence of shear heating along the slab (Fig. 5) on the development of these compositionally driven instabilities at moderate initial buoyancy ratio $R_\rho = 3.5$ (Models 1–4 in Table 2). The amount of shear heating employed is greatest in Fig. 5a, where shear heating along the length of the entire slab is accounted for and includes the brittle deformation field at temperatures lower than 600 K as well, intermediate in Fig. 5b, where only shear heating at temperatures greater than 600 K is included in the temperature equation, and no shear heating at all in Fig. 5c. A comparison of these three situations shows clearly the importance of
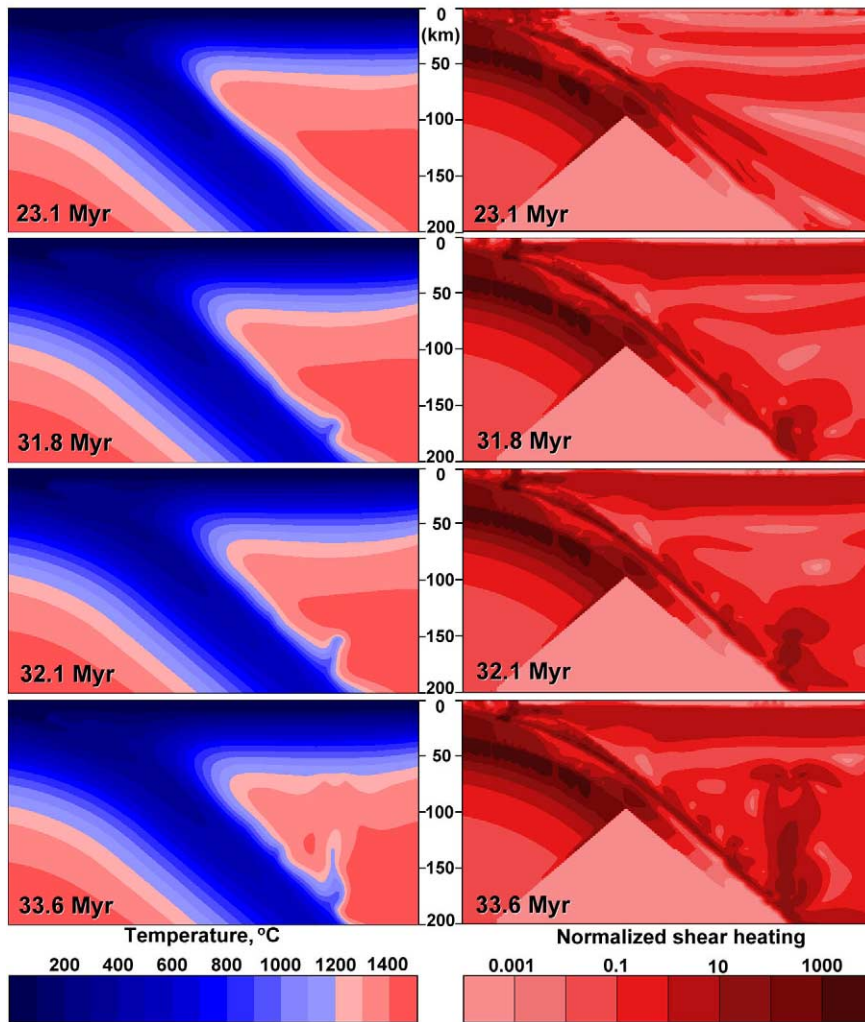
Fig. 4. Development of the temperature field (left column) and shear heating distribution (right column) of the model shown in Fig. 3. Shear heating has been normalized by heating due to radioactive elements present in peridotite (Table 1).

shear heating along the slab in promoting cold-plume generation, since in the case without shear heating the instability is hardly excited due to lowered temperature and increased viscosity of the dry mantle atop the hydrated zone. This comparison shows that at an initial value of $R_\rho = 3.5$ even a small addition of frictional heat at shallow depths within a subduction zone is crucial for the generation of the cold plumes. Taking into account a moderate amount of shear heating along the slab predicted by other models (e.g. [56]), more work is needed in studying the role of this

factor in the brittle regime and due to slab bending (e.g. [51]). Another possible source of heat at shallow depths may be the latent heat of the serpentinization of the mantle wedge, which is not considered here.

In Fig. 6 we show four examples illustrating the variations in the morphology of cold plumes with changing model parameters for numerical experiments with an initially high buoyancy ratio $R_\rho = 5.6$ (Models 5–10 in Table 2). The instability for these models develops much earlier at times of 19–21 Myr than for the reference model (Table 2).
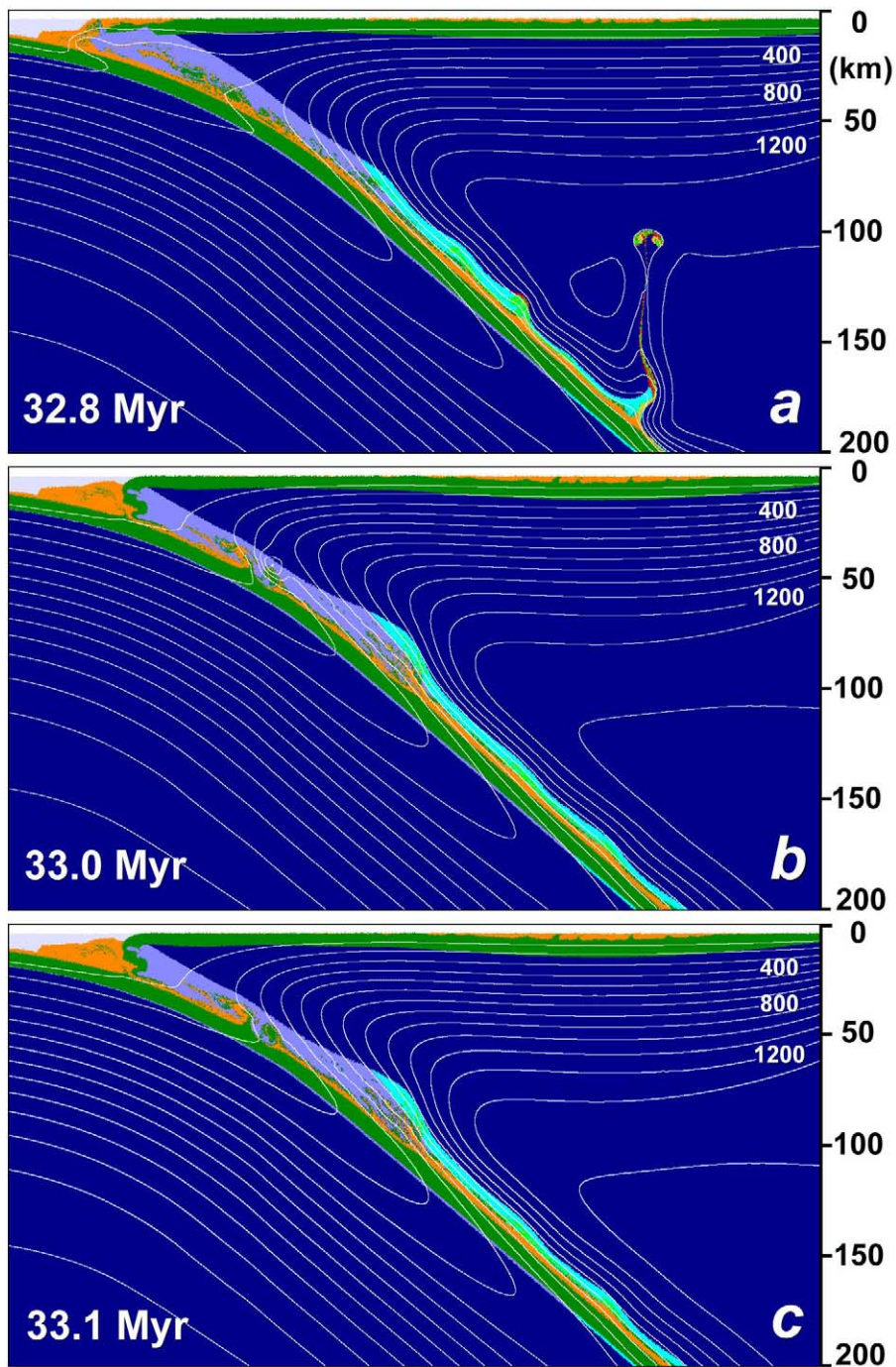
Fig. 5. Influence of viscous dissipation on the development of cold plumes in numerical experiments with moderate initial buoyancy ratio, $R_\rho = 3.5$ (Models 1–4 in Table 2). (a) Viscous heating is included at all temperatures (Model 1 in Table 2). (b) Viscous heating is accounted for only for temperatures above 600 K (Model 2 in Table 2). (c) No shear heating is considered (Model 3 in Table 2). Color code is the same as in Fig. 3.
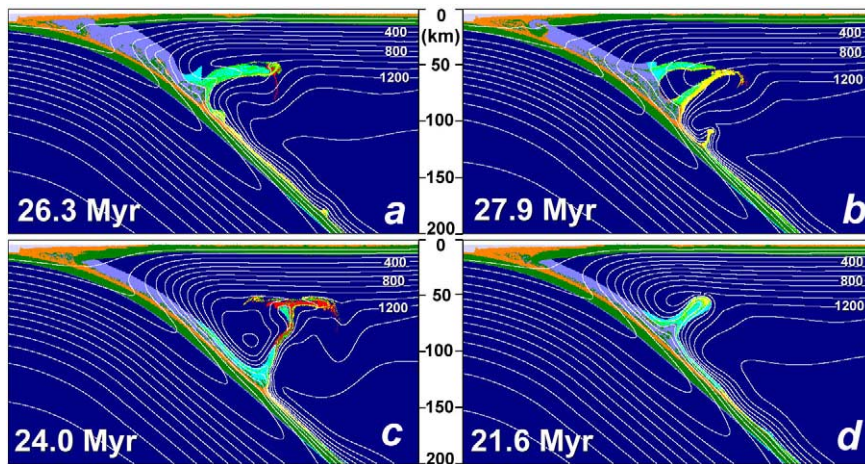
Fig. 6. Variations in the morphology of 'cold plumes' due to variations in model parameters for numerical experiments with high initial buoyancy ratio, $R_\rho = 5.6$ (Models 5–10 in Table 2). (a) Doubling the hydration rate (Model 6 in Table 2). (b) Younger lithospheric age of 60 Myr (Model 7 in Table 2). (c) No shear heating at all (Model 8 in Table 2). (d) Older lithospheric age of 100 Myr (Model 9 in Table 2). Color code is the same as in Fig. 3.

First, we test the sensitivity of the solution to a doubling of the hydration rate in Fig. 6a triggered by greater fluxing of hydrous fluids and resulting in a notably thicker serpentinized channel (light gray-blue). A cold plume propagates powerfully from the descending slab right under the lithosphere, leading to the possibility of underplating. Next, we study in Fig. 6b the influence of having a younger subducting lithosphere of 60 Myr. Many more instabilities than the reference model are developed, along with a thick serpenitized layer (light gray-blue). The tips of the two upwellings have different melting components, showing the diversity of the magmatic outcomes in this model. We show in Fig. 6c that for models with high initial buoyancy ratio the instability can also develop without shear heating. Without shear heating, the instabilities develop deeper down, leading to more melting of the peridotite (red color) inside the plume, due to the crossing of the wet peridotite solidus curve by the temperature field near the slab interface (cf. *P–T* diagram in Fig. 3). Finally, in Fig. 6d we look at the effects of an older age slab of 100 Ma. After 21.6 Myr the thermal–chemical instability reaches an apex characterized by a thick head filled with partially molten sediments and basalts embedded in hydrated peridotite. Afterwards this upwelling loses its po-

tency and is bent by the downward circulation. There is a great richness in the petrological possibilities of the melt developed in these thermal–chemical plumes.

8. Conclusions and perspectives

In this work we have demonstrated the dynamical feasibility for upwellings, around 300–400°C colder than the ambient mantle, to emerge from the top surface of the descending lithosphere and to pass through the mantle wedge. For subduction with 2 cm/yr a moderate initial density contrast of $\Delta\rho \geq 140$ kg/m^3 and corresponding buoyancy ratio $R_\rho \geq 3.5$ are needed to generate cold plumes from a self-organizing, 1–10 km thick, hydrated source layer formed along the subducting slab under the mantle wedge dominated by dry olivine dislocation flow-law rheology. These counter-intuitive cold hydrous plumes are powered primarily by compositional buoyancy, which is maintained by the presence of partially molten material due to melting triggered by fluxing of hydrous fluids released from many realistic [27] dehydration reactions, such as serpentine decomposition. These ascending plumes with diverse origins of melting components, are also lubricated by

a sheath of reduced-viscosity layer due to the heat produced by the large amount of viscous dissipation, which is caused by the efficient conversion of gravitational potential energy into mechanical dissipation [52–54]. In spite of the small dissipation number ($\sim$ 0.04) and the relatively short vertical trajectory (at most 200 km), these chemical plumes produce much more viscous heating than their thermal counterparts from the lower mantle.

The upward passage of these cold plumes would have important consequences for the thermomechanical evolution of subducting zones. First, they should penetrate rapidly through the hot asthenosphere in the mantle wedge and, second, this would cause local cooling. Instead of being interpreted as hot anomalies [12], the low seismic velocity anomalies [57] near Japan may be interpreted as having some water content [58]. Taking into account the presence of water bearing minerals, including serpentine, talk, amphiboles and chlorites [27], in relatively cold ($< 850°C$) zones of hydrated peridotite source layer, there may be a spatial correlation between seismicity and the particular depth of cold-plume initiation due to dehydration embrittlement (e.g. [14]) of ascending rocks.

The regional mantle circulation and the thermal structure developed in our numerical models are quite complex and differ significantly from those obtained by only considering thermal effects (e.g. [9,30,56]). Our findings truly illustrate the multi-scale nature of mantle convection by displaying another hierarchy of secondary plumes emerging from the slab, a primary boundary layer in mantle convection. Our results also appear to be more realistic when they are compared with the seismic data, revealing the complexity of seismological signatures in the vicinity of subduction zones, particularly near the Japanese trench area and at various depths (e.g. [12,14,57,59]). Therefore, we believe that our numerical approach and additional comparison with geophysical and petrological constraints may lead to a deeper understanding of the cause-and-effect relationships in the seismic and magmatic activities at convergent plate boundaries.

As discussed by Hall and Kincaid [11], the diapiric model agrees well with several important observations of magmatism at subduction zones, including the regularity in spacing between discrete volcanic centers (e.g. [12]) and rapid (within 0.03–0.12 Myr) upward transport of magmas from the subducted crust (e.g. [60]). Recent geophysical and geochemical studies have shown important variations in sources and transportation rates of magmas and fluids contributing to volcanic activities at subduction zones (e.g. [11,60,61]). Taking into account the variability of petrological components of cold plumes found in our numerical experiments, further high-resolution realistic numerical modeling is needed to reveal details of cold-plume morphology, composition and the dynamics of their initiation and propagation.

Besides the subducting slab, we may speculate further that similar 'cold plumes' can also be produced at much greater depths, such as the transition zone, a site for the development of secondary plumes (e.g. [6]). Another set of cold plumes can develop from the hydrated portions of deeply subducted or even detached slabs, lying atop the 660 km discontinuity. In summary, we argue strongly that a significant part of the magmatic and seismic activities in the Earth's interior may be related to development of cold plumes with compositional, hydrous origins. Therefore, we would need to investigate further this new, intrinsically non-linear phenomenon by a multi-faceted approach involving the combined efforts of seismology, rheology, petrology and numerical modeling, since there is a great sensitivity of the geological and geophysical outcomes to the various input parameters.

Acknowledgements

and S. Omori, concerning Japanese plate tectonics and other matters. We thank Lilli Yang for drawing Fig. 1. Constructive reviews by Jeroen van Hunen and Garrett Ito are greatly appreciated.*[RV]*

References

[1] P. Olson, I.S. Nam, Formation of seafloor swells by mantle plumes, J. Geophys. Res. 91 (1986) 7181–7191.

[2] D. Bercovici, J. Mahoney, Double flood basalts and plume head separation at the 660-kilometer discontinuity, Science 266 (1994) 1367–1369.

[3] S. Ni, D.V. Helmberger, Seismological constraints on the South African Superplume: could be the oldest distinct structure on Earth, Earth Planet. Sci. Lett. 206 (2003) 119–131.

[4] W.J. Morgan, Deep mantle convection plumes and plate motions, Am. Assoc. Petr. Geol. Bull. 56 (1972) 203–213.

[5] U. Hansen, D.A. Yuen, Numerical simulations of thermal-chemical instabilities and lateral heterogeneities at the core-mantle boundary, Nature 334 (1988) 237–240.

[6] L. Cserepes, D.A. Yuen, On the possibility of a second kind of mantle plume, Earth Planet. Sci. Lett. 183 (2000) 61–71.

[7] D.P. McKenzie, The relation between fault plane solutions for earthquakes and the directions of the principal stresses, Bull. Seismol. Soc. Am. 59 (1969) 591–601.

[8] B.D. Marsh, Island-arc development: some observations, experiments, and speculations, J. Geol. 87 (1979) 687–713.

[9] H.J. Davies, D.J. Stevenson, Physical model of source region of subduction zone volcanics, J. Geophys. Res. 97 (1992) 2037–2070.

[10] A. Gorbatov, J. Dominguez, G. Suarez, V. Kostoglodov, D. Zhao, E. Gordeev, Tomographic imaging of the P-wave velocity structure beneath the Kamchatka peninsula, Geophys. J. Int. 137 (1999) 269–279.

[11] P.S. Hall, C. Kincaid, Diapiric flow at subduction zones: A recipe for rapid transport, Science 292 (2001) 2472–2475.

[12] Y. Tamura, Y. Tatsumi, D.P. Zhao, Y. Kido, H. Shukuno, Hot fingers in the mantle wedge: new insights into magma genesis in subduction zones, Earth Planet. Sci. Lett. 197 (2002) 105–116.

[13] H. Iwamori, D.P. Zhao, Melting and seismic structure beneath the northeast Japan arc, Geophys. Res. Lett. 27 (2000) 425–428.

[14] T. Seno, D. Zhao, Y. Kobayashi, M. Nakamura, Dehydration of serpentinized slab mantle: Seismic evidence from southwest Japan, Earth Planets Space 53 (2001) 861–871.

[15] L.H. Rüpke, J.P. Morgan, M. Hort, J.A.D. Connolly, Are the regional variations in Central American arc lavas due to differing basaltic versus peridotitic slab sources of fluids?, Geology 30 (2002) 1035–1038.

[16] T.V. Gerya, D.A. Yuen, Rayleigh-Taylor instabilities drive 'cold plumes' at subduction zones, EOS Trans. AGU 83(47), Fall Meet. Suppl., Abstract T22A-1140 (2002).

[17] E.R. Oxburgh, D.L. Turcotte, Origin of paired metamorphic belts and crustal dilation in island arc regions, J. Geophys. Res. 76 (1971) 1315–1327.

[18] A. Hsui, M.N. Töksöz, The evolution of thermal structures beneath a subduction zone, Tectonophysics 60 (1979) 43–60.

[19] P. Ulmer, V. Trommsdorff, Serpentine stability to mantle depths and subduction related magmatism, Science 268 (1995) 858–861.

[20] U. Hansen, D.A. Yuen, Nonlinear physics of double-diffusive convection in geological systems, Earth Sci. Rev. 29 (1990) 385–399.

[21] D.L. Turcotte, G. Schubert, Geodynamics: Applications of Continuum Physics to Geological Problems, Wiley, New York, 1982, 430 pp.

[22] D. Bittner, H. Schmeling, Numerical modeling of melting processes and induced diapirism in the lower crust, Geophys. J. Int. 123 (1995) 59–70.

[23] C. Clauser, E. Huenges, Thermal conductivity of rocks and minerals, in: T.J. Ahrens (Ed.), Rock Physics and Phase Relations, AGU Reference Shelf 3, AGU, Washington, DC, 1995, pp. 105–126.

[24] G. Ranalli, Rheology of the Earth, 2nd edn., Chapman and Hall, London, 1995, 413 pp.

[25] T.V. Gerya, B. Stoeckhert, A.L. Perchuk, Exhumation of high-pressure metamorphic rocks in a subduction channel - a numerical simulation, Tectonics 21 (2002) 6-1–6-19.

[26] W. Johannes, The significance of experimental studies for the formation of migmatites, in: V.A. Ashworth (Ed.), Migmatites, Blackie, Glasgow, 1985, pp. 36–85.

[27] M.W. Schmidt, S. Poli, Experimentally based water budgets for dehydrating slabs and consequences for arc magma generation, Earth Planet. Sci. Lett. 163 (1998) 361–379.

[28] S. Poli, M.W. Schmidt, Petrology of subducted slabs, Annu. Rev. Earth Sci. 30 (2002) 207–235.

[29] C. Kincaid, I.S. Sacks, Thermal and dynamic evolution of the upper mantle in subduction zones, J. Geophys. Res. 102 (1997) 12295–12315.

[30] J. van Hunen, A.P. van den Berg, N.J. Vlaar, A thermomechanical model of horizontal subduction below an overriding plate, Earth Planet. Sci. Lett. 182 (2000) 157–169.

[31] K. Regenauer-Lieb, D.A. Yuen, J. Branlund, The initiation of subduction: critically by addition of water?, Science 294 (2001) 578–580.

[32] S. Zhong, M. Gurnis, Mantle convection with plates and mobile, faulted plate margins, Science 267 (1995) 838–843.

[33] D.J. Stevenson, J.S. Turner, Angle of subduction, Nature 270 (1977) 334–336.

[34] A. Tovish, G. Schubert, B.P. Luyendyk, Mantle flow

pressure and the angle of subduction: non-Newtonian cornerflows, J. Geophys. Res. 83 (1978) 5892–5898.

[35] D.L. Turcotte, G. Schubert, Frictional heating of the descending lithosphere, J. Geophys. Res. 78 (1973) 5876–5886.

[36] A.N.B. Poliakov, Y. Podladchikov, Diapirism and topography, Geophys. J. Int. 109 (1992) 553–564.

[37] M. Gurnis, C. Eloy, S. Zhong, Free-surface formulation of mantle convection - II. Implication for subduction-zone observables, Geophys. J. Int. 127 (1996) 719–727.

[38] S.M. Peacock, Serpentinization and infiltration metasomatism in the Trinity peridotite, Klamath province, northern California: implications for subduction zones, Contrib. Mineral. Petrol. 95 (1987) 55–70.

[39] H. Bureau, H. Keppler, Complete miscibility between silicate melts and hydrose fluids in the upper mantle: experimental evidence and geochemical implications, Earth Planet. Sci. Lett. 165 (1999) 187–196.

[40] M. Scambelluri, P. Philippot, Deep fluids in subduction zones, Lithos 55 (2001) 213–227.

[41] B. Schott, H. Schmeling, Delamination and detachment of a lithospheric root, Tectonophysics 296 (1998) 225–247.

[42] W.F. Brace, D.L. Kohlestedt, Limits on lithospheric stress imposed by laboratory experiments, J. Geophys. Res. 85 (1980) 6248–6252.

[43] B. Stöckhert, J. Renner, Rheology of crustal rocks at ultrahigh-pressure, in: B.R. Hacker, J.G. Liou (Eds.), When Continents Collide: Geodynamics and Geochemistry of Ultrahigh-Pressure Rocks, Kluwer Academic, Dordrecht, 1998, pp. 57–95.

[44] B. Stöckhert, Stress and deformation in subduction zones - insight from the record of exhumed high pressure metamorphic rocks, in: S. de Meer, M. Drury, H. de Bresser, G. Pennock (Eds.), Deformation Mechanisms, Rheology, and Tectonics: Current Status and Future Perspectives, Geol. Soc. London Spec. Publ. 200, 2002, pp. 255–274.

[45] H. Pinkerton, R.J. Stevenson, Methods of determining the rheological properties of magmas at subliquidus temperatures, J. Volcanol. Geotherm. Res. 53 (1992) 47–66.

[46] D.R. Scott, D.J. Stevenson, Magma ascent by porous flow, J. Geophys. Res. 91 (1986) 9283–9296.

[47] J.A.D. Connolly, Yu.Yu. Podladchikov, Compact-driven fluid flow in viscoelastic rock, Geodin. Acta (Paris) 11 (1998) 55–84.

[48] O.V. Vasilyev, Y.Y. Podladchikov, D.A. Yuen, Modeling of compaction driven flow in poro-viscoelastic medium using adaptive wavelet collocation method, Geophys. Res. Lett. 25 (1998) 3239–3243.

[49] T.V. Gerya, D.A. Yuen, Characteristics-based marker method with conservative finite-differences schemes for modeling geological flows with strongly variable transport properties, Phys. Earth Planet. Inter. (submitted).

[50] T. Nakagawa, P.J. Tackley, Thermo-chemical structure in the mantle arising from a three-component convective system and implications for geochemistry, Phys. Earth Planet. Inter. (2003) (in press).

[51] C.P. Conrad, B.H. Hager, The thermal evolution of an earth with strong subduction zones, Geophys. Res. Lett. 26 (1999) 3041–3044.

[52] U. Hansen, D.A. Yuen, Formation of layered structures in double-diffusive convection as applied to the Geosciences, in: Double-Diffusive Convection, Geophysical Monograph 94, AGU, Washington, DC, 1995, pp. 135–149.

[53] U. Hansen, D.A. Yuen, Potential role played by viscous heating in thermal-chemical convection in the outer-core, Geochim. Cosmochim. Acta 60 (1996) 1113–1123.

[54] V.P. Myasnikov, Y.Y. Podladchikov, D.A. Yuen, Heat-transfer properties of thermal-chemical convection and implications on the thermal histories of terrestial planets, EOS Trans. AGU Fall Meet. Suppl., Abstract, 1999.

[55] J.A. Conder, D.A. Wiens, J. Morris, On the decompression melting structure at volcanic arcs and back-arc spreading centers, Geophys. Res. Lett. 29 (2002) 17-1–17-4.

[56] S.M. Peacock, Blueschist-facies metamorphism, shear heating, and P-T-t paths in subduction shear zones, J. Geophys. Res 97 (1992) 17693–17707.

[57] D.P. Zhao, O.P. Mishra, R. Sandra, Influence of fluid and magma on earthquakes: seismological evidence, Phys. Earth Planet. Inter. 132 (2002) 249–267.

[58] H. Jung, S. Karato, Water-induced fabric transitions in olivine, Science 293 (2001) 1460–1463.

[59] S. Omori, T. Komabayashi, S. Maruyama, Depth distribution of the subduction zone earthquakes and devolatilization phase equilibria of subducting slab, EOS Trans. AGU 83(47), Fall Meet. Suppl., Abstract T22C-03, 2002.

[60] C.J. Hawkesworth, S.P. Turner, F. McDermott, D.W. Peate, P. van Calsteren, U-Th isotopes in arc magmas implications for element transfer from the subducted crust, Science 276 (1997) 551–555.

[61] T.L. Grove, S.W. Parman, S.A. Bowring, R.C. Price, M.B. Baker, The role of an H2O-rich fluid component in the generation of primitive basaltic andesites and andesites from the Mt. Shasta region, N California, Contrib. Mineral. Petrol. 142 (2002) 375–396.